The Astrophysical Journal, 678:262–273, 2008 May 1

COMPOSITION OF PRIMARY COSMIC-RAY NUCLEI AT HIGH ENERGIES

M. Ave, P. J. Boyle,[1] F. Gahbauer,[2] C. Höppner,[3] J. R. Hörandel,[4]
M. Ichimura,[5] D. Müller, and A. Romero-Wolf[6]
Enrico Fermi Institute, University of Chicago, 933 East 56th Street, Chicago, IL 60637; boyle@uchicago.edu
Received 2007 September 14; accepted 2008 January 3

ABSTRACT

The TRACER instrument (Transition Radiation Array for Cosmic Energetic Radiation) has been developed for direct measurements of the heavier primary cosmic-ray nuclei at high energies. The instrument had a successful long-duration balloon flight in Antarctica in 2003. The detector system and measurement process are described, details of the data analysis are discussed, and the individual energy spectra of the elements O, Ne, Mg, Si, S, Ar, Ca, and Fe (nuclear charge $Z = 8$–26) are presented. The large geometric factor of TRACER and the use of a transition radiation detector make it possible to determine the spectra up to energies in excess of 10^{14} eV per particle. A power-law fit to the individual energy spectra above 20 GeV amu^{-1} exhibits nearly the same spectral index (2.65 ± 0.05) for all elements, without noticeable dependence on the elemental charge Z.

Subject headings: acceleration of particles — cosmic rays — ISM: abundances — methods: data analysis

Online material: color figures

1. INTRODUCTION

The energies of cosmic rays observed near Earth extend over a very wide range, from below 10^8 eV to more than 10^{20} eV per particle. Up to about 10^{10} eV amu^{-1}, the particle energies and intensities are significantly affected by solar modulation, but for the nearly 10 remaining decades, the arriving particles are believed to represent the ambient cosmic-ray population in the local Galaxy. Over this range, the total cosmic-ray intensity (the "all particle" differential energy spectrum; see, for instance, the compilation of Cronin et al. 1997) decreases monotonically by more than 30 orders of magnitude, initially as a power law $\propto E^{-2.7}$, steepening slightly to $E^{-3.0}$ at the "knee" above 10^{15} eV per particle, and exhibiting small changes in slope again (a "second knee" and an "ankle") in the 10^{18}–10^{19} eV region. Besides these relatively minor changes, the overall spectrum is remarkably featureless, even though a variety of processes may contribute to the cosmic-ray flux. The general consensus is that the particles below the knee are generated inside our Galaxy and are contained by the Galactic magnetic fields for millions of years, while at the highest energies ($\geq 10^{18}$ eV) the gyration radii become so large that Galactic containment is no longer effective, and that the cosmic rays may then be of extragalactic origin.

The all-particle energy spectrum refers to the overall spectrum of cosmic rays without differentiating the individual components. To obtain deeper insight, details of the composition of the cosmic-ray particles must be studied. For instance, very accurate measurements of not only the elemental, but also the isotopic composition are now available at low energies ($\leq 10^9$–10^{10} eV per particle). The abundances of radioactive clock nuclei such as Be^{10} led to the average containment time in the Galaxy of $\tau \approx 1.5 \times 10^7$ yr at these energies (Garcia Muñoz et al. 1975; Yanasak et al. 2001), and the relative abundances of Co and Ni isotopes excluded fresh supernova ejecta as source material of cosmic rays (Wiedenbeck et al. 1999). At relativistic energies, only the abundances of the elemental species, without isotopic detail, have been accessible to measurements (e.g., Engelmann et al. 1990), but even these encounter increasingly severe systematic and statistical uncertainties as the energy increases. Very few direct observations (e.g., Müller et al. 1991) have provided composition detail with single-element resolution above 10^{13} eV per particle. The work described in this paper represents an attempt to improve this situation and to determine the energy spectra of individual elemental species up to much higher energies.

The current paradigm of the origin of Galactic cosmic rays postulates first-order Fermi acceleration in interstellar shock fronts from supernova (SN) explosions as the most potent contributor to the cosmic-ray flux below the knee. This mechanism, first proposed by Bell (1978), must be very efficient indeed, since as much as ~10% of the total kinetic energy released in supernova explosions is required to sustain the cosmic-ray flux. The SN shock acceleration mechanism predicts a source energy spectrum in the form of a power law $\propto E^{-\Gamma}$, with a spectral index $\Gamma \approx 2.0$ for strong shocks. Such a spectrum is much harder than the $E^{-2.7}$ spectrum that seems to be typical for most primary cosmic-ray nuclei below the knee. This difference in spectral slope can be explained if the propagation and containment of cosmic rays in the Galaxy are energy-dependent. Such a behavior had indeed been inferred, even before the SN shock acceleration model was formulated, on the basis of measurements of the "L/M ratio"; i.e., of the abundance of secondary, spallation-produced cosmic rays (such as the light elements Li, Be, B) relative to their primary parents (such as C and O) (Juliusson et al. 1972). One concludes from such measurements that the average amount of interstellar matter encountered by cosmic-ray nuclei during their propagation through the Galaxy decreases with energy. The effect is often parameterized by a propagation path length Λ, which depends on energy as $\Lambda \propto E^{-0.6}$ for relativistic nuclei (Engelmann et al. 1990). The primary cosmic-ray spectrum at the source would then be approximately $\propto E^{-2.1}$ or $E^{-2.2}$, close to what the shock acceleration model predicts. This fact provides strong but indirect evidence for the validity of the shock acceleration model.

However, it must be kept in mind that current measurements of the L/M ratio do not extend beyond 10^{11} eV amu^{-1} (or about

[1] Corresponding author
[2] Current address: University of Latvia, Latvia.
[3] Current address: Technische Universität München, Germany.
[4] Current address: Radboud University Nijmegen, The Netherlands.
[5] Current address: Hirosaki University, Japan.
[6] Current address: University of Hawaii.

10^{12} eV per particle). Hence, there is an extended region of energies (10^{12}–10^{15} eV per particle) where the SN shock acceleration model is assumed to be valid, albeit without the benefit of much observational support. The SN shock acceleration process is expected to become inefficient at energies around $Z \times 10^{14}$ eV (where Z is the atomic number of a cosmic-ray nucleus) (Lagage & Cesarsky 1983), but this limit is not observationally confirmed. One might refer to the steepening of the all-particle spectrum at the "knee" as evidence, but even then the origin of cosmic rays with energies far beyond the knee remains a mystery.

The SN shock acceleration model has recently found strong observational support through the detection of TeV gamma rays from shell-type SN remnants (Aharonian et al. 2004), although there remains debate about whether the parent particles of these gamma rays are electrons or, indeed, protons and nuclei (for a detailed discussion, see, e.g., Berezhko & Völk 2006).

Clearly, the present observational evidence about high-energy cosmic rays is inadequate to provide answers to some of the most fundamental questions about their origin and Galactic propagation, and there exists an undeniable need for improved measurements at higher energies. The TRACER (Transition Radiation Array for Cosmic Energetic Radiation) program has been developed to provide direct measurements of the energy spectra of the heavier cosmic-ray nuclei through balloon flights above the atmosphere, up to energies between 10^{14} and 10^{15} eV per particle. Higher energies are currently studied through indirect observations with ground-based air shower installations. However, attempts to obtain composition details from air shower observations are affected by a number of systematic uncertainties. One of the goals of TRACER is to approach the energy region of air shower measurements, with the hope of providing some cross-calibration with the indirect measurements.

2. OBSERVATIONAL TECHNIQUE

2.1. *General Principles*

A successful cosmic-ray measurement above the atmosphere must determine at least two quantities for each particle: the charge Z and the energy E. Measurement of Z is commonly accomplished by utilizing the fact that all electromagnetic interactions scale with Z^2. Hence, devices that measure the ionization energy loss (dE/dx), such as plastic scintillators or gas proportional counters, or that measure the intensity of Cerenkov light, are well suited to and are used in TRACER.

The energy determination is a greater challenge, mainly because of the large detector areas that are needed at high energy. Extrapolations from lower energies indicate that a successful measurement of nuclei heavier than helium requires detectors with exposure factors of at least several 100 m^2 sr days in order to approach the 10^{15} eV per particle region. Such exposures can be accomplished with long-duration (i.e., several week) balloon flights if the detectors have sensitive areas of a few square meters. A classic calorimeter that measures the total energy absorbed in matter after a particle interacts would become much too massive if it were to have an area of this magnitude.

Hence, TRACER uses electromagnetic interactions not just to determine Z, but also to measure the energy (or more exactly, the Lorentz factor $\gamma \approx E/mc^2$): measurement of Cerenkov light produced in an acrylic Cerenkov counter at low energies (up to a few 10^9 eV amu^{-1}), measurement of the specific ionization in gases at intermediate energies (10^{10}–10^{12} eV amu^{-1}), and measurement of transition radiation at the highest energies (>4×10^{11} eV amu^{-1}).

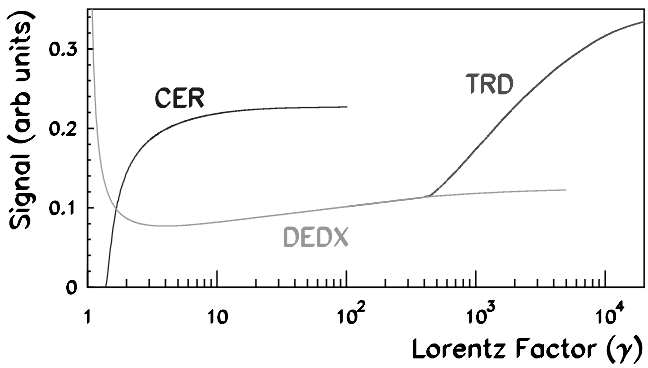

FIG. 1.—Energy response of detection techniques used in TRACER: Cerenkov counter (CER), energy loss in gases (DEDX), and transition radiation detection (TRD). [*See the electronic edition of the Journal for a color version of this figure.*]

Figure 1 shows the typical energy responses for the detectors used in TRACER. The light intensity of an acrylic Cerenkov counter (refractive index = 1.49) increases quickly with energy above a threshold of 0.325 GeV amu^{-1} ($\gamma \approx 1.35$) until it approaches saturation above 20 GeV amu^{-1} ($\gamma \approx 22$). The ionization loss in gas decreases with energy, reaches a minimum at $\gamma = 3.96$, and then increases logarithmically with E. Transition radiation (TR) X-rays are generated in a multisurface radiator (mats of plastic fibers in TRACER) and are detected in a gas proportional counter. Hence, the TR detector measures an ionization loss signal, and at sufficiently high energies (>4×10^{11} eV amu^{-1}), a superimposed signal due to the absorption of TR photons. The TR signal rises rapidly with the Lorentz factor γ and reaches saturation in the $\gamma = 10^4$–10^5 region. The use of TR to measure the highest cosmic-ray energies was first implemented for the Cosmic Ray Nuclei (CRN) detector in 1985 (L'Heureux et al. 1990), but remains unconventional. It permits the construction of detectors of very large area. As the TR intensity increases with Z^2, this technique is well suited for measurements of the heavier cosmic rays ($Z > 3$), but is not applicable to protons or He nuclei, where the signals are affected by large statistical fluctuations.

Note that the response curves shown in Figure 1 for the detectors of specific ionization and TR are double-valued: large signals can either be produced by high-energy particles, or by particles below minimum ionization. At regions with low geomagnetic cutoff energies, where TRACER must fly, a significant cosmic-ray intensity arrives with subrelativistic energies. The inclusion of a plastic Cerenkov counter that identifies the low-energy particles is then essential in order to remove the degeneracy of ionization and TR response. Overall, the counter combination chosen for TRACER measures the energies of cosmic-ray nuclei over a very wide range, in excess of 4 orders of magnitude.

2.2. *The TRACER Instrument*

A schematic cross section of the TRACER instrument is shown in Figure 2. The detector elements are rather large in area (206 × 206 cm) and are vertically separated by 120 cm. This leads to an overall geometric factor of about 5 m^2 sr. The instrument has been described previously (Gahbauer et al. 2004), and a detailed technical description of the detector elements is currently being prepared for a separate publication. Here we present a brief summary of the relevant properties of the instrument.

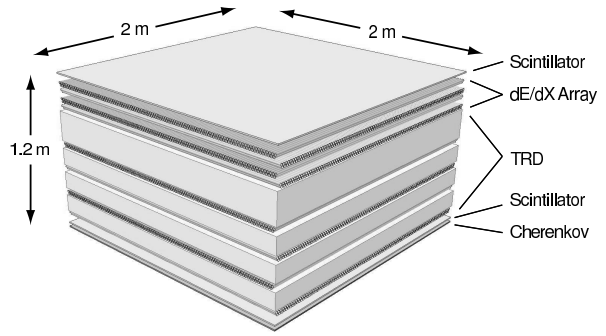

FIG. 2.—Schematic drawing of TRACER. [*See the electronic edition of the Journal for a color version of this figure.*]

As Figure 2 shows, the individual components of TRACER are, from top to bottom:

1. A plastic scintillator sheet (BICRON-408 material) with an active area 200×200 cm, and 0.5 cm thick.[7] The scintillator is viewed by 24 photomultiplier tubes (PMTs) via wavelength shifter bars.
2. Four double layers of single-wire proportional tubes, oriented in two orthogonal directions. Each tube is 200 cm long and 2 cm in diameter. The tube walls are wound from aluminized Mylar and are about 127 μm thick.
3. Another four double layers of proportional tubes of identical design, but each double layer located below blankets of plastic fiber material, which form a radiator to generate transition radiation.

All tubes are filled with a mixture of xenon and methane (at equal parts by volume) and are operated in flight at a pressure of 0.5 atm.

4. A second scintillator of identical design, but read out by just 12 PMTs, and located below the lowest layer of proportional tubes.
5. A Cerenkov counter, with an active area 200×200 cm and 1.27 cm thick, at the bottom of the detector stack. The Cerenkov material consists of an acrylic plastic (refractive index = 1.49), doped with wavelength shifter material. Signals are read out via wavelength shifter bars connected to 24 PMTs (as with the scintillator on top).

The two scintillators serve as triggers for the instrument and, together with the Cerenkov counter, determine the elemental charge Z of individual cosmic-ray nuclei traversing the instrument. The proportional counter arrays measure the energy (or Lorentz factor $\approx E/mc^2$) of the cosmic-ray particles at high energies, and they determine the trajectory of each particle traversing the instrument in two projections. The signals in the top four double layers are simply a measure for the ionization energy loss (dE/dx) of the particle. The small logarithmic increase above the minimum ionization level provides an estimate of the particle energy up to Lorentz factors of a few hundred. The lower four double layers of tubes form a transition radiation detector (TRD). As the response curves in Figure 1 show, the TRD signals are identical to the dE/dx signals of the tubes above, except at the highest energies ($\gamma > 400$), where the rapid increase of the signal with increasing γ permits an energy measurement. The signals of the proportional tubes (a total of about 1600) are processed through VLSI chips (Amplex; Beuville et al. 1990). The finite dynamic range of these devices restricts the range of elemental species for which data could be recorded in this flight, from oxygen ($Z = 8$) to iron ($Z = 26$).

[7] Due to the interspersed wavelength shifter bars, the geometric area of these counters is slightly larger than the active area.

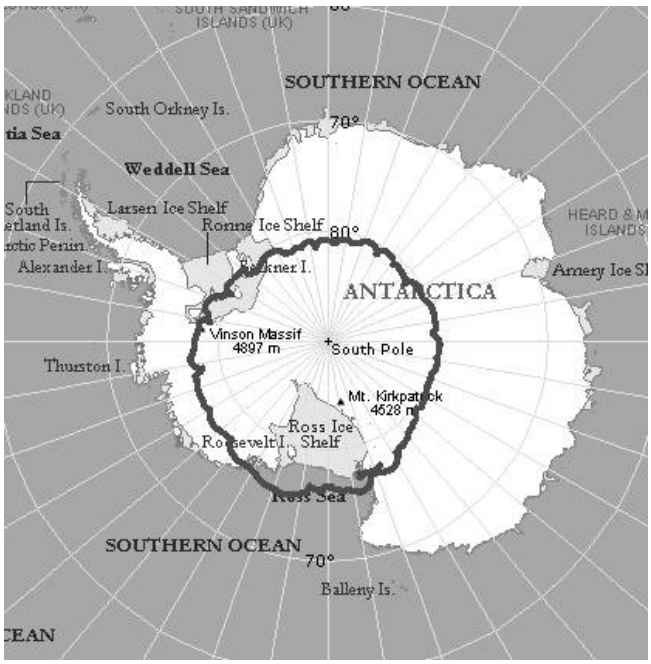

FIG. 3.—Trajectory of 2003 TRACER Antarctic long-duration balloon flight. [*See the electronic edition of the Journal for a color version of this figure.*]

The TRACER instrument derives its heritage from the CRN detector that was developed by our laboratory in the 1980s for space flight (L'Heureux et al. 1990). In fact, the radiator material used for the TRACER TRD is identical to that of the CRN. However, the CRN employed thin-window multiwire proportional chambers to detect transition radiation, and hence needed a heavy pressurized container. The proportional tubes used in TRACER instead can easily withstand external low pressure; and thus, a pressurized gondola is not required nor used for TRACER.

3. BALLOON FLIGHT AND INSTRUMENT PERFORMANCE

TRACER first had a 1 day balloon flight in Fort Sumner, New Mexico, in 1999. The results from this flight have been published (Gahbauer et al. 2004). A circumpolar long-duration balloon (LDB) flight was originally planned in the Northern Hemisphere with a launch from Alaska, but could not be conducted, because of the lack of relevant international agreements. Therefore, an LDB flight had to be planned in Antarctica, but had to wait until 2003, when a new launch vehicle commensurate with the weight of TRACER (6000 lbs., including ballast, telemetry, and balloon-related instrumentation) became operational. TRACER was launched near McMurdo, Antarctica, on 2003 December 12. During its 2 week flight (see Fig. 3) at an average height of 37.75 km (3.9 g cm^{-2}) with excursions not exceeding ± 1.75 km, it collected data from a total of 5×10^7 cosmic-ray events. The data were transmitted at 500 Mbits s^{-1} to the ground (when the instrument was within telemetry range) and stored on six disks on board and recovered after termination of the flight.

Overall, the instrument performed very well during this flight. In particular, the entirely passive thermal insulation kept the temperatures of all detector components close to room temperature, with diurnal variations of at most a few degrees Celsius. There

was no indication of a deterioration of the performance of the proportional tubes due to gas poisoning for the duration of the flight. This result would be of great practical importance if flights of such devices for much longer duration (for instance in space) are anticipated: there seems to be no need for gas purging at the timescales of at least a few weeks, except for the provision of makeup gas to correct for minor gas leaks. The data acquisition system operated very efficiently, with a dead time of just 6%, but the total time during which data could be recorded was limited to 10 days, due to a catastrophic failure of the rechargeable lithium batteries (which were used to buffer the solar power system) toward the end of the first orbit of the balloon around the South Pole.

4. DATA ANALYSIS

4.1. *Trajectory Reconstruction*

The first step in the analysis of the data is the accurate reconstruction of the trajectory of each cosmic-ray particle through the instrument. The entire array of proportional tubes is used for this purpose. It consists of four double layers of tubes in each the x- and y-direction. Hence, ideally a trajectory is characterized by eight tube "hits" in each projection. In practice, sometimes the particle may pass between adjacent tubes of a given layer and not generate a hit in this layer. In addition, spurious signals in tubes outside the particle trajectory may be recorded.

As a first estimate, the path is obtained using the center of each of the tubes hit in an event. All possible combinations of these tubes are fit with straight lines in the x- and y-projection, and the combination in each projection with minimum χ^2 per degree of freedom and maximum number of tubes used is kept. This method allows an accuracy of 5 mm in track position. The procedure is quite efficient: less than 5% of cosmic-ray nuclei are missed in the process.

A preliminary estimate of the charge of each particle is then performed using the technique described in the following section. A subset of the data from which we expect the same average signal in any tube (high-energy O or Ne nuclei) is then used to correct for deviations of the tube positions from their "ideal" positions, and to match signal gains within 5% or less. Corrections due to variations in the tube gain with time due to either temperature changes or small gas leakages are also calculated and applied. In general, gain variations in a given tube are negligible *along* that tube. Finally, the tube signals are corrected to account for minor nonlinearities in the front-end electronics at large signals. All these corrections are necessary to reduce the systematic uncertainties in the tube signals below the level of unavoidable physical fluctuations ("Landau fluctuations") in the energy deposited in the gas.

As a final step, the trajectory is refined by using the fact that the energy deposit in each tube is proportional to the track length in that tube. Taking this fact into account, an accuracy of 2 mm in the lateral track position is achieved, which corresponds to a 3% uncertainty in the total path length through all the tubes. The accuracy and efficiency of this method are verified with a GEANT4 simulation (Agostinelli et al. 2003) of the instrument.

The accurate knowledge of the particle trajectories is essential to the analysis, for two reasons: first, it permits corrections of the scintillator and Cerenkov signals due to spatial nonuniformities and zenith-angle variations (see § 4.2). Second, it makes it possible to determine accurately the average energy deposit of a cosmic-ray particle when it traverses the tubes. Specifically, the average signals are as follows.

In the top four double layers, the average specific ionization is defined as

$$\left\langle \frac{dE}{dx} \right\rangle = \frac{\sum_{i=1}^{i=8} \Delta E_i}{\sum_{i=1}^{i=8} \Delta x_i}, \tag{1}$$

and in the bottom four double layers (which form the TRD), the average signal is

$$\left\langle \frac{dE}{dx} + \mathrm{TR} \right\rangle = \frac{\sum_{i=9}^{i=16} \Delta E_i}{\sum_{i=9}^{i=16} \Delta x_i}, \tag{2}$$

where ΔE_i and Δx_i refer to energy deposit and path length, respectively, in tube number i. The two quantities defined in equations (1) and (2) are, of course, identical within fluctuations at energies where no transition radiation is detectable (TR = 0). In order to exclude large fluctuations associated with short path lengths, we remove tubes with $\Delta x_i < 1$ cm from the summation.

4.2. *Charge Analysis*

As a first step to determine the charge of each particle, the signal recorded by each PMT is corrected to account for the spatial nonuniformities in the counter responses. These corrections are derived using the tracking information together with response maps recorded with muons at ground and verified with the flight data themselves in an iterative procedure. Subsequently, for each event the average signal of all PMTs in each counter is calculated and then normalized to vertical incidence. Figure 4 shows a scatter plot of the *top* scintillator signal versus the Cerenkov signal. It is apparent that particles with the same charge are clustered along lines. The position along the line depends on the primary energy: a concentration of events around maximum Cerenkov and minimum scintillation signals corresponds to energies of minimum ionizing particles and above, and the energies decrease for events toward the left of this concentration.

The scintillator signals depend on particle charge as $Z^{1.65}$, due to nonlinear effects in the light yield, while the Cerenkov signals follow the expected Z^2 dependence. The residual scintillation in the Cerenkov counter is visible in Figure 4 and is subtracted out in the analysis. Figure 5 shows a charge histogram for all charges obtained from summing along lines of constant charge in Figure 4. The charge resolution evolves from 0.25 charge units for $Z = 8$ (O nuclei) to 0.5 charge units for $Z = 26$ (Fe nuclei) at low energies (<10 GeV amu^{-1}), and increases slightly to 0.3 and 0.6 charge units, respectively, at the highest energies.

Note that Figure 5 is generated just on the basis of the signals of the top scintillator, and thus depicts a histogram of Z_{top}. One can, in the same fashion, construct a histogram of Z_{bot}, using the signals of the bottom scintillator. For the further analysis, we require that Z_{top} and Z_{bot} are consistent within fluctuations for each accepted event. In practice, this means that particles with $Z_{\mathrm{bot}} < Z_{\mathrm{top}}$ are rejected. In almost all cases, these are particles that have undergone a nuclear spallation while traversing the detector material between the top and bottom of the instrument (for numerical detail, see § 5 and Fig. 10).

The procedure to select a sample of a given element for further analysis is as follows: first, with a very tight cut on Z_{bot}, clean, penetrating nuclei are selected, and their distribution in Z_{top} is investigated. This yields the values for charge resolution mentioned above, and it indicates the efficiency if a charge cut on Z_{top} is made. If the cut on Z_{top} is of the order of $\Delta Z_{\mathrm{top}} \geq \pm 0.5$ charge units, the efficiency is quite high. For certain elements, a tighter

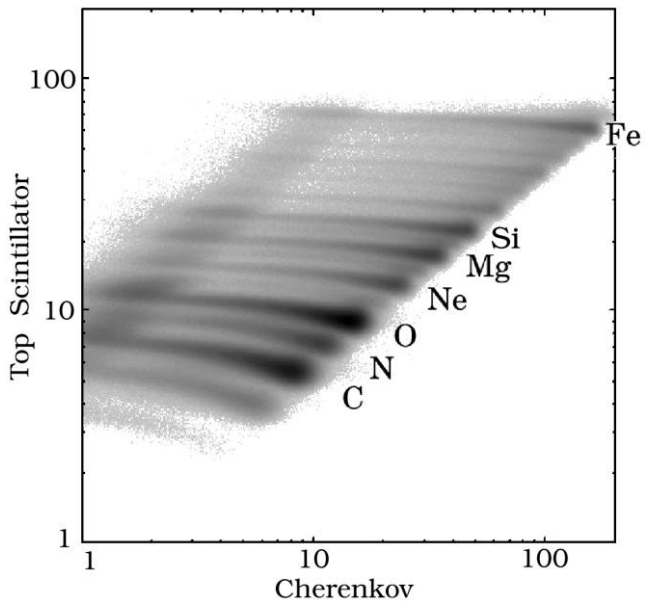

FIG. 4.—Scatter plot of top scintillator vs. Cerenkov signals in arbitrary units.

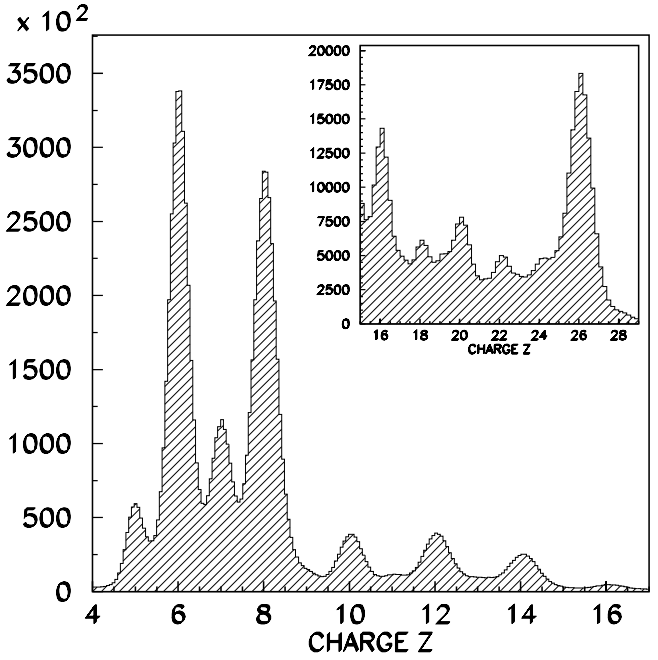

FIG. 5.—Charge histogram for all events measured in flight.

cut on $Z_{\rm top}$ must be made, and the efficiency is then reduced. Numerical details are given in § 5 and Table 1. It should be noted that the tight cut on $Z_{\rm bot}$ is only applied in order to determine the form of the charge distribution on $Z_{\rm top}$. For the final analysis, only a very loose cut on $Z_{\rm bot}$ is used to remove interacting particles. This cut leads to a negligible reduction in overall charge selection efficiency.

Finally, it should be noted that "edge" effects can compromise the charge resolution. To avoid this problem, tracks with an impact point within 1 cm of the wavelength shifter bars are excluded. This creates a dead area in the detector of about 4% of the total area.

4.3. *Energy Analysis*

4.3.1. *Overview*

The energy of each cosmic-ray nucleus is obtained from the combined signals of the Cerenkov counter and of the proportional tubes. The top four double layers of tubes measure the specific ionization of each particle, $\langle dE/dx\rangle$, while the bottom four double layers detect transition radiation, measuring $\langle dE/dx + {\rm TR}\rangle$. While the main objective of the Cerenkov counter is to identify low-energy particles, below the level of minimum ionization, the rapid increase of the signal with energy provides a good energy measurement up to about 3 GeV amu^{-1}.

At energies between minimum ionization and the onset of TR (3–400 GeV amu^{-1}), the signals in the *dE/dx* tubes and the TR tubes are the same and increase logarithmically with energy. This increase is slow and can be used for an energy measurement unless it is obscured by statistical signal fluctuations. The relative level of the fluctuations decreases with the nuclear charge as $1/Z$. Therefore, the energy measurement improves with increasing Z. Note that each individual proportional tube provides an estimate for the specific ionization by measuring the ratio $\Delta E_i/\Delta x_i$. Hence, for any particle, up to 16 tubes provide independent measurements, and these are required to be consistent within fluctuations. For the final analysis, the average $\langle dE/dx\rangle$, as defined in equations (1) and (2), is used.

At the highest energies (>400 GeV amu^{-1}), the signals from the *dE/dx* tubes and from the TR tubes diverge, and the rapid increase of the TR signals with particle energy provides an excellent energy measurement. However, particles in this energy region are extremely rare, being less abundant than particles in the minimum ionization region by more than 4 orders of magnitude. To uniquely identify these particles, it is necessary but not sufficient to just require that low-energy nuclei are rejected on the basis of their Cerenkov signals. In addition, we require that the measurement of their ionization energy loss $\langle dE/dx\rangle$ (performed with four double layers of *dE/dx* tubes) places them at an energy level well above minimum ionization (for details, see § 4.3.3 and Table 2). Thus, the combination of *dE/dx* tubes with the TRD tubes is crucial for the success of the TRACER measurement at the highest energies.

4.3.2. *Identification of Subrelativistic Particles* (*<3 GeV amu^{-1}*)

To identify low-energy particles, the signals from the Cerenkov counter are compared with those of the *dE/dx* tubes. The *dE/dx* response, shown in Figure 1, is well described by the Bethe-Bloch formula. The Cerenkov counter response (Fig. 1) must be slightly modified to account for effects of δ-rays generated by the primary particle in the instrument, while the signals from the proportional tube array remain unaffected by δ-rays. These effects are well understood and have been previously studied and reported (Gahbauer

TABLE 1
CHARGE SELECTION EFFICIENCIES

Element	8	10	12	14	16	18	20	26
Cut (charge units)	±0.5	±0.5	±0.5	±0.5	±0.1	±0.1	±0.1	±1.0
Efficiency.....	0.89	0.83	0.75	0.72	0.17	0.18	0.18	0.90

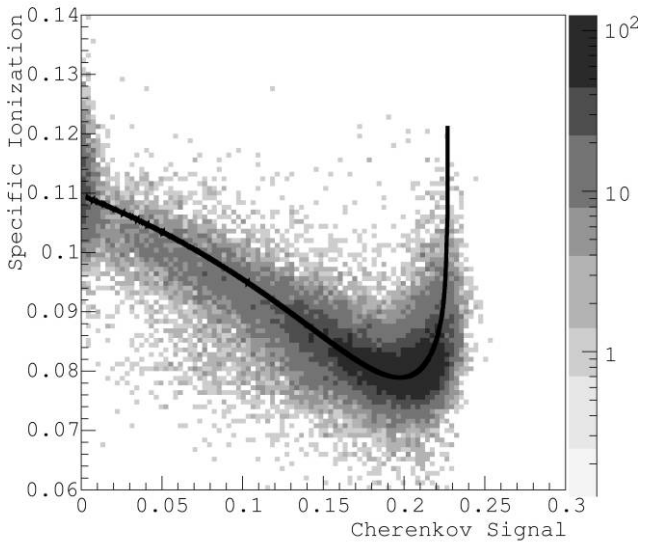

FIG. 6.—Scatter plot of *dE/dx* vs. Cerenkov signals for iron nuclei. The black line is the average response obtained from simulations. The gray scale is logarithmic.

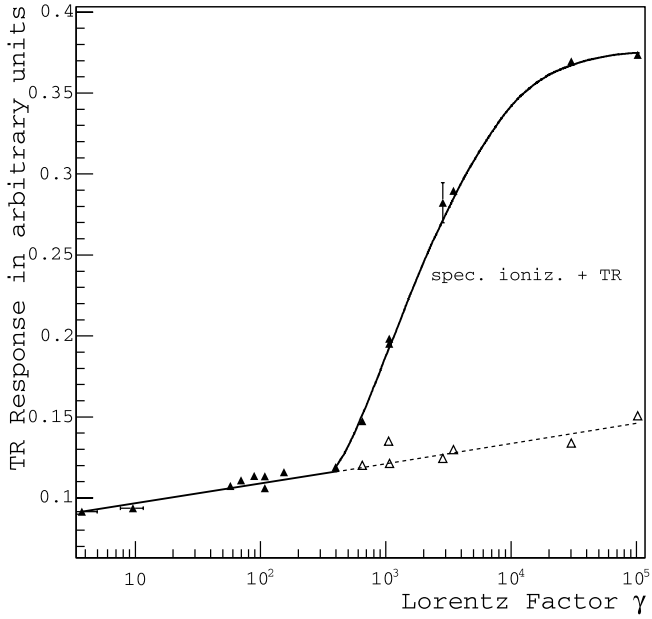

FIG. 7.—Energy response of the TRD as measured at accelerators. Except for two highest energy data points, these measurements have been published previously (L'Heureux et al. 1990). The open symbols and dashed lines refer to measurements of *dE/dx* only.

et al. 2003; Romero-Wolf 2005). The scatter plot in Figure 6 shows the correlation of the ionization and Cerenkov signals measured for iron nuclei. The solid line represents the average response expected from simulations. The Cerenkov signal increases with energy until it reaches saturation, while the ionization signal clearly exhibits the level of minimum ionization ($\sim$3 GeV amu^{-1}). Note that the gray scale of the scatter plot is logarithmic. Plots like this one for each charge exhibit the level of fluctuations in the Cerenkov signal: it is about 8% for O nuclei and 2.5% for Fe nuclei. A cut in the Cerenkov signal is placed at a level that corresponds to the minimum in the ionization signal. Events with Cerenkov signals below this cut are used to generate their energy spectrum from 0.8 to 2.3 GeV amu^{-1}. Events with Cerenkov signals above the cut are used to construct the energy spectra above 12 GeV amu^{-1}, as described in the following section.

4.3.3. *High-Energy Particles*

After removing all particles below about 3 GeV amu^{-1}, the rare high-energy particles are identified from the combination of the signals from the *dE/dx* tubes and the TRD. These detectors have been calibrated at accelerators using singly charged particles. Figure 7 shows the measured response for the TRD of the CRN instrument (L'Heureux et al. 1990). The radiator combination and gas mixtures of TRACER are identical to those of the CRN instrument. However, the CRN used planar multiwire proportional chambers rather than the layers of cylindrical proportional tubes of TRACER. We have ascertained in Monte Carlo simulations that the accelerator calibrations for the CRN remain valid for the detector geometry of TRACER. Most of the data shown in Figure 7 have been published previously (L'Heureux et al. 1990).

Below 400 GeV amu^{-1}, we expect no observable transition radiation. Both signals, $\langle dE/dx \rangle$ and $\langle dE/dx + \mathrm{TR} \rangle$, increase logarithmically with energy and will cluster along the diagonal in a correlation plot of TRD response versus ionization response, as illustrated in Figure 8. Above 400 GeV amu^{-1}, TR becomes observable, and the signal from the TRD will increase above the ionization signal. This manifests itself as a deviation from the diagonal in the correlation plot.

As an example, Figure 9 shows the observed cross-correlation between the TRD and the ionization signals for neon nuclei ($Z =$ 10) above minimum ionization. The small black points represent the numerous events with energies below the onset of TR. The rare high-energy particles with clear TR signals are highlighted. As expected, the data follow the response illustrated in Figure 8. Note that the highest energy events (the "TR events") stand out without any background in other regions of the scatter plot. The most energetic neon nucleus in this sample of data has an energy of 6×10^{14} eV.

We must emphasize again that the off-diagonal position of these higher energy events defines them uniquely as TR events for the selected charge ($Z = 10$ in Fig. 9). Any spillover due to misidentified charges, with Z either larger or smaller than the selected value,

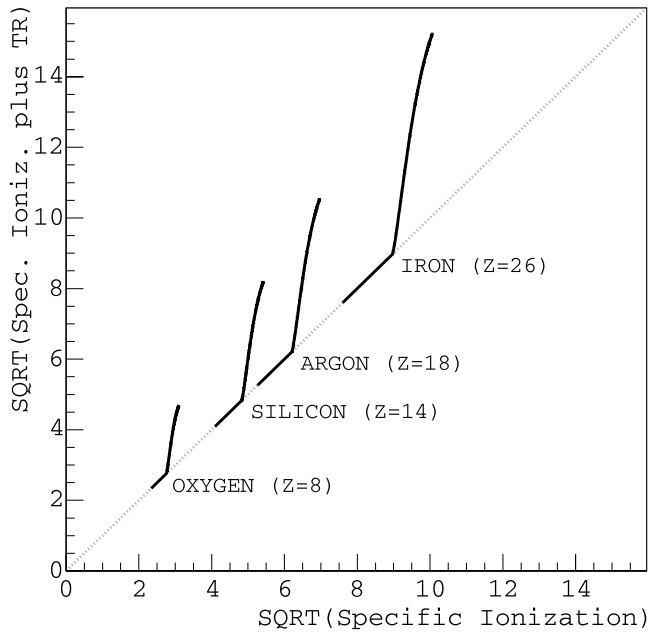

FIG. 8.—Correlation of average responses (square root) of TR and specific ionization detectors for relativistic nuclei. Four elements are displayed to illustrate the charge dependence of the responses.

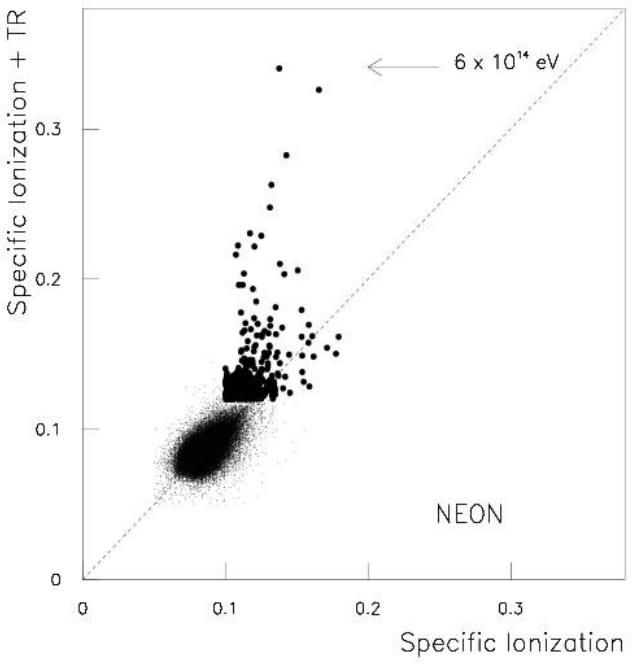

FIG. 9.—Scatter plot of TR vs. *dE/dx* signal for neon nuclei. The highlighted points represent the highest energy events measured with the TRD. As expected, the transition radiation events have signals in the *dE/dx* detector that are well above the minimum ionization level. Units are arbitrary.

would lead to signals along the diagonal, but would not contaminate the well-defined "TR tails."

5. ABSOLUTE FLUX MEASUREMENTS

Each event that passes the data analysis cuts is classified in energy as either a "Cerenkov event" (<3 GeV amu^{-1}), a "*dE/dx* event" (10–400 GeV amu^{-1}), or a "TR event" (>400 GeV amu^{-1}). Events are sorted into energy bins of width ΔE_i, and a differential energy spectrum is constructed for each elemental species. We present the spectra in terms of an absolute flux dN/dE at the top of the atmosphere. To convert from the number of events ΔN_i in a particular energy bin ΔE_i to an absolute differential flux $dN/dE(i)$, one must compute the exposure factor, effective aperture, and efficiency of the cuts, and unfold the instrument response:

$$\frac{dN}{dE}(i) = \frac{\Delta N_i}{\Delta E_i}\left(\frac{1}{T_l}\right)\left(\frac{1}{\varepsilon_i}\right)\left(\frac{1}{A_i}\right)C_i \qquad (3)$$

where ΔN_i is the number of events, ΔE_i the energy range, T_l the live time, ε_i the efficiency of analysis cuts, A_i the effective aperture, and C_i the "overlap correction" due to misidentified events from neighboring energy bins. For Cerenkov events, one also must take into account that ΔE_i, the energy interval on top of the atmosphere, is not equal to the measured energy interval, because of energy losses in the atmosphere and in the detector.

The quantities used here are obtained as follows:

Live time.—The live time is determined by comparing the raw trigger rate with the number of events stored on disk. At a raw trigger rate of 60–80 Hz, and a dead time of 6%, the total live time is 787,200 s.

Tracking efficiency.—The efficiency of the track fit is 95% for all charges and is independent of energy. Included is a consistency check in the signal of the tubes contributing to the $\langle dE/dx\rangle$ and $\langle dE/dx + \mathrm{TR}\rangle$ measurements.

Charge efficiency.—For the more abundant elements (O, Ne, Mg, Si) a charge cut of $Z_{\mathrm{top}} \pm 0.5$ is made. The efficiencies range from 85% to 72% (O, Si) and are listed in Table 1. For the less abundant elements (S, Ar, Ca), a more conservative cut of $Z_{\mathrm{top}} \pm 0.1$ is imposed to avoid contamination from adjacent charges, which yields a reduced efficiency of 17%. For iron, a cut of $Z_{\mathrm{top}} \pm 1.0$ is used at an efficiency of 90%. The consistency cut on the charge at the bottom of the instrument, Z_{bot}, is sufficiently loose to not affect the overall efficiency.

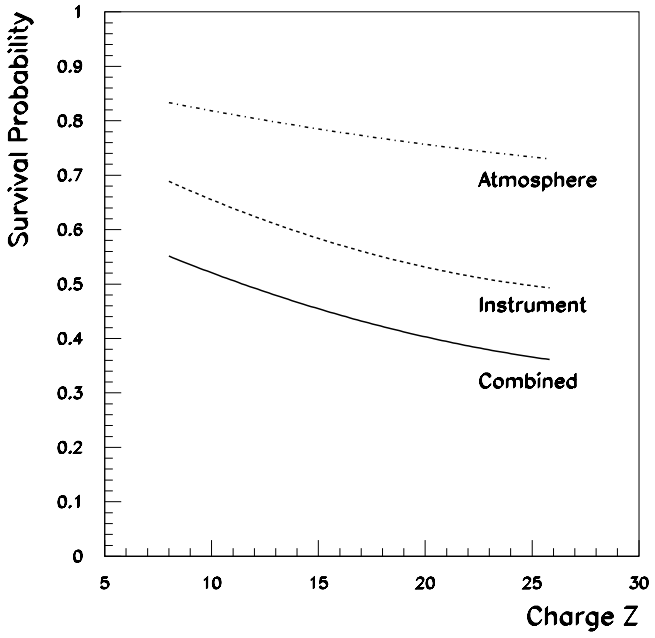

FIG. 10.—Survival probability of all nuclei incident at a zenith angle of 30° in a residual atmosphere of 3.91 g cm^{-2} (*dash-dotted line*), within the TRACER instrument (*dashed line*), and total survival probability (*solid line*).

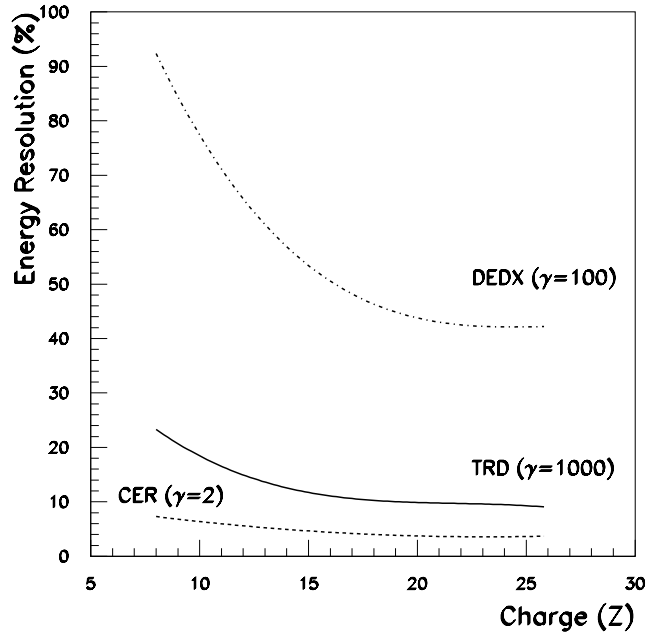

FIG. 11.—Energy resolution (1 σ) of individual detector subsystems vs. charge Z and for typical energies: Cerenkov: $\gamma = 2$ (*dashed line*), *dE/dx*: $\gamma = 100$ (*dash-dotted line*), and TRD: $\gamma = 1000$ (*solid line*).

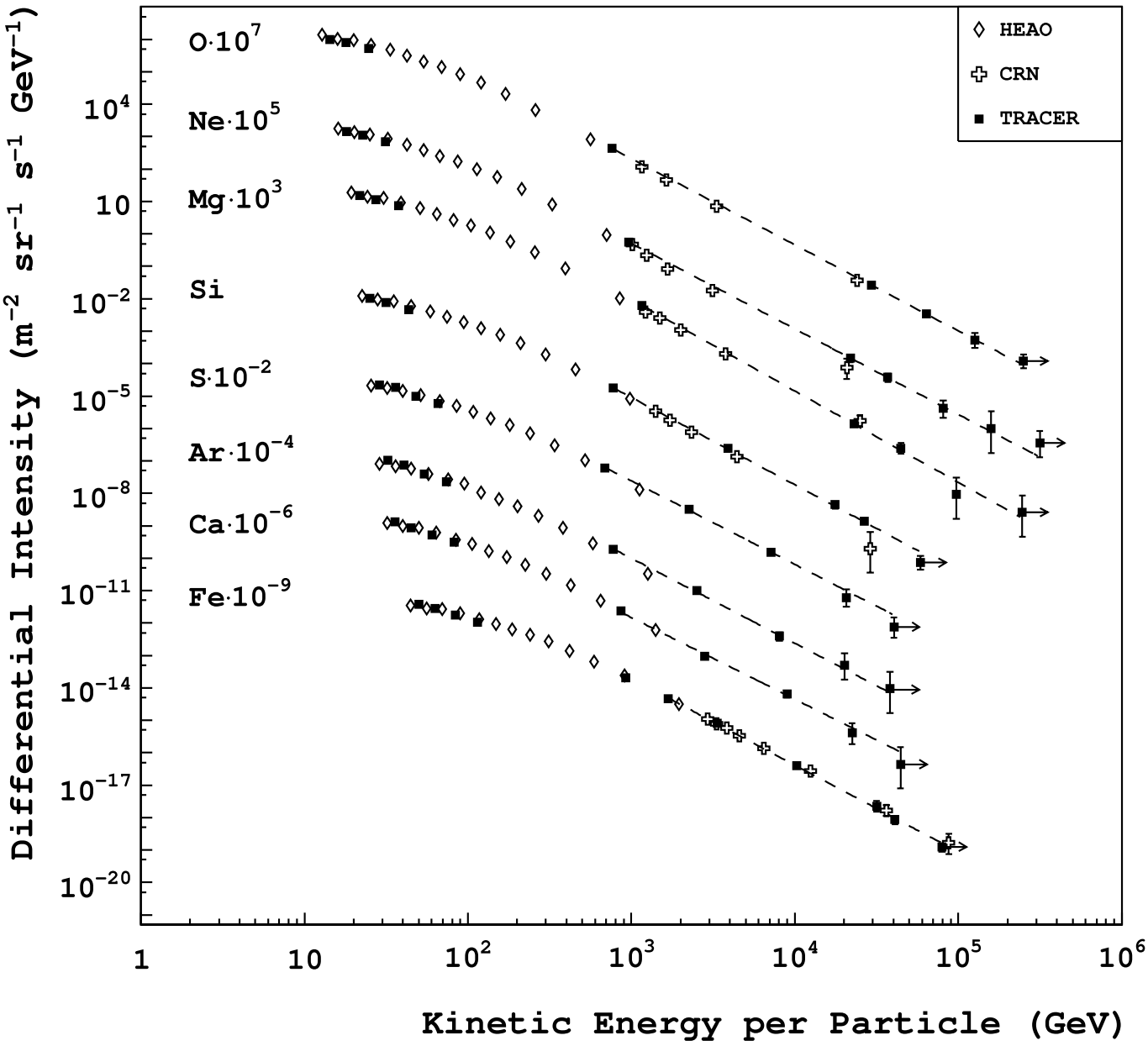

FIG. 12.—Differential energy spectra vs. energy per particle of the cosmic-ray nuclei: O, Ne, Mg, Si, S, Ar, Ca, and Fe. Results from the TRACER 2003 flight are indicated by the filled squares. Existing data from the HEAO-3 experiment (*open diamonds*; Engelmann et al. 1990) and the CRN experiment (*open crosses*; Müller et al. 1991) are shown for comparison. The dashed line represents an independent power-law fit to each spectrum above 20 GeV amu^{-1}. [*See the electronic edition of the Journal for a color version of this figure.*]

Effective aperture.—The overall geometric factor of TRACER is 5.04 m^2 sr. For the flux computation, an effective aperture A_i is calculated, which includes the geometric factor, losses due to nuclear spallations, and "dead" regions in the detector:

$$A_i = A2\pi \int_{\theta=0}^{\pi/2} P_I(\theta) P_D(\theta) \cos\theta \, d(\cos\theta) \qquad (4)$$

where A is the area of the detector (206 × 206 cm), $P_I(\theta)$ the probability of survival against spallation in the atmosphere and in the instrument as a function of zenith angle θ (see Fig. 10), and $P_D(\theta)$ is the probability that a particle passing through the top scintillator will traverse the entire instrument without encountering any insensitive detector regions. The quantity $P_D(\theta)$ is determined from a Monte Carlo simulation. Insensitive detector regions lead to a reduction in the overall geometric factor by about 10%.

Losses due to nuclear interactions are computed using a combination of measured charge-changing cross sections and parameterizations obtained by Heckmann et al. (1978) and Westfall et al. (1979). The interaction losses are taken to be independent of energy but do depend on the particle mass. Interactions in the atmosphere are determined by measuring the residual atmosphere above the payload, which for this flight was monitored by pressure sensors and GPS modules attached to the instrument. The average residual atmosphere was 3.91 g cm^{-2}. Interaction probabilities in the instrument are obtained by numerical computation using a complete list of materials in TRACER. The fraction of interacting nuclei in

TABLE 2
MEASURED INTENSITIES (OXYGEN-SILICON)

Element	Energy Range (GeV amu^{-1})	Kinetic Energy[1] $\hat{E}$ (GeV amu^{-1})	Number of Events	Differential Intensity (m^2 s sr GeV amu^{-1})$^{-1}$
O ($Z = 8$).....	0.8–1.0	0.9	25,437	$(1.71 \pm 0.01) \times 10^{0}$
	1.0–1.3	1.1	24,237	$(1.38 \pm 0.01) \times 10^{0}$
	1.3–1.9	1.5	38,226	$(8.95 \pm 0.05) \times 10^{-1}$
	12–292	48	456,918	$(7.27 \pm 0.01) \times 10^{-4}$
	1315–2627	1834	77	$(4.4 \pm 0.5) \times 10^{-8}$
	2627–6371	4001	29	$(5.8 \pm 1.1) \times 10^{-9}$
	6371–9834	7872	5	$(9.1^{+6.0}_{-3.9}) \times 10^{-10}$
	9834–	15,611	6	$(2.0^{+1.2}_{-0.8}) \times 10^{-10}$
Ne ($Z = 10$).....	0.8–1.0	0.9	4031	$(3.08 \pm 0.05) \times 10^{-1}$
	1.0–1.3	1.1	3790	$(2.42 \pm 0.04) \times 10^{-1}$
	1.3–1.9	1.5	5639	$(1.48 \pm 0.02) \times 10^{-1}$
	12–292	48	57,991	$(1.21 \pm 0.01) \times 10^{-4}$
	895–1316	1080	16	$(3.2 \pm 0.8) \times 10^{-8}$
	1316–2627	1834	13	$(8.2 \pm 2.3) \times 10^{-9}$
	2627–6371	4001	4	$(8.9^{+6.9}_{-4.2}) \times 10^{-10}$
	6371–9834	7872	1	$(2.2^{+5.0}_{-1.8}) \times 10^{-10}$
	9834–	15,611	2	$(7.8^{+10.1}_{-5.0}) \times 10^{-11}$
Mg ($Z = 12$).....	0.8–1.0	0.9	4603	$(4.02 \pm 0.06) \times 10^{-1}$
	1.0–1.3	1.1	4184	$(2.96 \pm 0.05) \times 10^{-1}$
	1.3–1.9	1.5	6339	$(1.89 \pm 0.02) \times 10^{-1}$
	12–292	48	59,374	$(1.60 \pm 0.01) \times 10^{-4}$
	696–1316	946	23	$(3.6 \pm 0.7) \times 10^{-8}$
	1316–2627	1834	9	$(6.3^{+2.9}_{-2.1}) \times 10^{-9}$
	2627–6371	4001	1	$(2.4^{+5.6}_{-2.0}) \times 10^{-10}$
	6371–	10,113	1	$(6.7^{+15.4}_{-5.5}) \times 10^{-11}$
Si ($Z = 14$).....	0.8–1.0	0.9	3127	$(3.07 \pm 0.06) \times 10^{-1}$
	1.0–1.3	1.1	2812	$(2.27 \pm 0.04) \times 10^{-1}$
	1.3–1.9	1.5	4292	$(1.39 \pm 0.02) \times 10^{-1}$
	12–73	28	36,369	$(5.23 \pm 0.03) \times 10^{-4}$
	73–292	138	2278	$(7.2 \pm 0.2) \times 10^{-6}$
	567–696	627	18	$(1.3 \pm 0.3) \times 10^{-7}$
	696–1316	946	24	$(4.0 \pm 0.8) \times 10^{-8}$
	1316–	2088	6	$(2.2^{+1.3}_{-0.9}) \times 10^{-9}$

[1] See text for definition of $\hat{E}$.

the instrument can also be obtained experimentally from a comparison of the reconstructed nuclear charges for each element in the top and bottom scintillators. Both methods lead to consistent results. As an example, an oxygen or iron nucleus at an incident angle of 30° has a probability of survival in the atmosphere of 83% or 73%, respectively, and probability of survival in the instrument of 70% or 49%, respectively (see Fig. 10 for all elements).

Energy overlap corrections.—As TRACER has three detectors, each with a different energy response and energy resolution (see Figs. 1 and 11), the widths of the energy intervals into which the data are sorted must be appropriately chosen. The intrinsic relative signal fluctuations decrease with increasing Z, essentially as $1/Z$ (Fig. 11). Therefore, the number of acceptable energy bins increases for elements with higher charge number.

As the shape of the energy spectra is not expected to vary rapidly with energy, choosing too fine a subdivision of the energy scale might just lead to increased statistical uncertainty in each energy bin, and hence not improve the quality of the results. More importantly, the widths of the bins must be commensurate with the energy resolution of the detector. Otherwise, overlap corrections for events being misinterpreted from a neighboring energy bin would become substantial and could possibly bias the result for a steeply falling spectrum.

In the current analysis of the TRACER data, the bin widths are chosen to be fairly wide, such that the overlap correction factor can be determined with the help of an iterative Monte Carlo simulation. The corrections are computed for each energy bin and element. They are fairly small, in general $\leq 20\%$ (i.e., $0.8 \leq C_i \leq 1.2$).

6. MEASURED ENERGY SPECTRA

The analysis yields, for each species, numbers of events ΔN_i sorted into energy bins $\Delta E_i = E_{i+1} - E_i$. The ratio $\Delta N_i/\Delta E_i$ defines the differential intensity dN/dE for this interval:

$$\frac{dN}{dE}(i) = \frac{\Delta N_i}{\Delta E_i}. \tag{5}$$

We assume that the energy spectrum is represented by a power law $CE^{-\alpha}$ over this interval, such that

$$\Delta N_i = \int_{E_i}^{E_{i+1}} CE^{-\alpha}\, dE. \tag{6}$$

We then plot the spectral value $dN/dE(i)$ at an energy level $\hat{E}$, defined such that

$$\frac{dN}{dE} = C\hat{E}^{-\alpha}, \tag{7}$$

TABLE 3
MEASURED INTENSITIES (SULPHUR-IRON)

Element	Energy Range (GeV amu^{-1})	Kinetic Energy[1] $\hat{E}$ (GeV amu^{-1})	Number of Events	Differential Intensity (m^2 s sr GeV amu^{-1})$^{-1}$
S ($Z = 16$).....	0.8–1.0	0.9	156	$(7.5 \pm 0.6) \times 10^{-2}$
	1.0–1.3	1.1	158	$(6.3 \pm 0.5) \times 10^{-2}$
	1.3–1.8	1.5	170	$(3.3 \pm 0.3) \times 10^{-2}$
	1.8–2.3	2.0	106	$(2.0 \pm 0.2) \times 10^{-2}$
	12–41	21	1212	$(2.1 \pm 0.1) \times 10^{-4}$
	41–130	70	212	$(1.1 \pm 0.1) \times 10^{-5}$
	130–412	223	32	$(5.2 \pm 0.9) \times 10^{-7}$
	529–792	644	4	$(2.1^{+1.6}_{-1.0}) \times 10^{-8}$
	792–	1257	3	$(2.6^{+2.5}_{-1.4}) \times 10^{-9}$
Ar ($Z = 18$).....	0.8–1.0	0.9	70	$(4.0 \pm 0.5) \times 10^{-2}$
	1.0–1.3	1.1	61	$(2.9 \pm 0.4) \times 10^{-2}$
	1.3–1.8	1.5	66	$(1.5 \pm 0.2) \times 10^{-2}$
	1.8–2.3	2.0	39	$(8.9 \pm 1.4) \times 10^{-3}$
	12–41	21	454	$(7.1 \pm 0.3) \times 10^{-5}$
	41–130	70	85	$(3.8 \pm 0.4) \times 10^{-6}$
	130–412	223	11	$(1.5 \pm 0.5) \times 10^{-7}$
	452–696	558	2	$(1.9^{+2.5}_{-1.3}) \times 10^{-8}$
	696–	1105	1	$(3.2^{+7.3}_{-2.6}) \times 10^{-9}$
Ca ($Z = 20$).....	0.8–1.0	0.9	99	$(5.5 \pm 0.6) \times 10^{-2}$
	1.0–1.3	1.1	79	$(3.7 \pm 0.4) \times 10^{-2}$
	1.3–1.8	1.5	99	$(2.2 \pm 0.2) \times 10^{-2}$
	1.8–2.3	2.0	61	$(1.3 \pm 0.2) \times 10^{-2}$
	12–41	21	610	$(9.9 \pm 0.4) \times 10^{-5}$
	41–130	70	88	$(4.1 \pm 0.4) \times 10^{-6}$
	130–412	223	19	$(2.8 \pm 0.6) \times 10^{-7}$
	452–696	558	3	$(1.8^{+1.7}_{-1.0}) \times 10^{-8}$
	696–	1105	1	$(1.9^{+4.3}_{-1.6}) \times 10^{-9}$
Fe ($Z = 26$).....	0.8–1.0	0.9	1821	$(2.21 \pm 0.05) \times 10^{-1}$
	1.0–1.3	1.1	1669	$(1.65 \pm 0.04) \times 10^{-1}$
	1.3–1.8	1.5	2166	$(1.02 \pm 0.02) \times 10^{-1}$
	1.8–2.3	2.0	1388	$(6.2 \pm 0.2) \times 10^{-2}$
	12–23	16	10,589	$(1.22 \pm 0.02) \times 10^{-3}$
	23–41	30	4468	$(2.80 \pm 0.04) \times 10^{-4}$
	41–92	60	2132	$(4.7 \pm 0.1) \times 10^{-5}$
	92–412	183	543	$(1.9 \pm 0.1) \times 10^{-6}$
	529–606	566	9	$(1.3^{+0.6}_{-0.4}) \times 10^{-7}$
	606–895	733	12	$(5.2 \pm 1.5) \times 10^{-8}$
	895–	1421	11	$(7.4 \pm 2.2) \times 10^{-9}$

[1] See text for definition of $\hat{E}$.

where

$$\hat{E} = \frac{1}{(E_{i+1} - E_i)} \frac{1}{(1-\alpha)} (E_{i+1}^{1-\alpha} - E_i^{1-\alpha})^{-1/\alpha}. \quad (8)$$

Since $\hat{E}$ depends on the value of α, an iterative procedure has been used. It is found that the dependence of $\hat{E}$ on α is not very strong.

For the spectra presented in this work, the highest energy intervals are integral bins, with $E_{i+1} \rightarrow \infty$. We then plot the data point at the median energy for this bin, $\hat{E}_{\rm int}$:

$$\hat{E}_{\rm int} = [E_i^{1-\alpha}/2]^{1/1-\alpha}. \quad (9)$$

The value of the flux at this energy is

$$\left|\frac{dN}{dE}\right|_{\rm int} = \frac{\Delta N_i(\alpha - 1)}{E_i^{1-\alpha}} \hat{E}_{\rm int}^{-\alpha}. \quad (10)$$

The energy spectra, in terms of absolute intensities, for the elements O, Ne, Mg, Si, S, Ar, Ca, and Fe are presented in Tables 2 and 3 and are plotted in Figure 12. The low-energy data points ($\leq$2.3 GeV amu^{-1}) come from an analysis of the Cerenkov counter, using a restricted angular acceptance. Note that the energy in the table is given in units of kinetic energy per amu, whereas in Figure 12 the units are given in terms of kinetic energy per particle. Data from the 2003 TRACER flight are indicated by the filled squares. For clarity, the intensity of each element is scaled by a factor shown on the left. Existing data from measurements in space with HEAO-3 (Engelmann et al. 1990) and the CRN (Müller et al. 1991) are shown for comparison. In the energy regions where overlap exists, the agreement of the results appears to be quite good.

We note the large range in intensity (10 decades) and particle energy (four decades) covered by TRACER. As can be seen, the energy spectra extend up to and beyond 10^{14} eV. The eight elements for which spectra are shown in Figure 12 represent the major primary species from oxygen to iron; contributions to these species from spallation-produced secondary elements are expected to be small. We can fit the high-energy part (>20 GeV amu^{-1}) of each spectrum to a power law in energy $E^{-\alpha}$. The resulting spectral indices are shown in Figure 13. Remarkably, there is no significant trend of the spectral indices with charge Z, and all indices

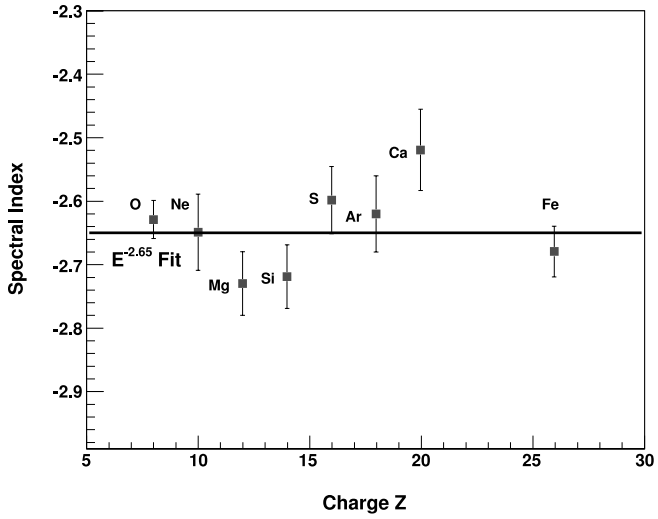

FIG. 13.—Spectral indices of a best power-law fit to the combined TRACER and CRN data above 20 GeV amu^{-1}. The line indicates an average spectral fit of $E^{-2.65}$. [*See the electronic edition of the Journal for a color version of this figure.*]

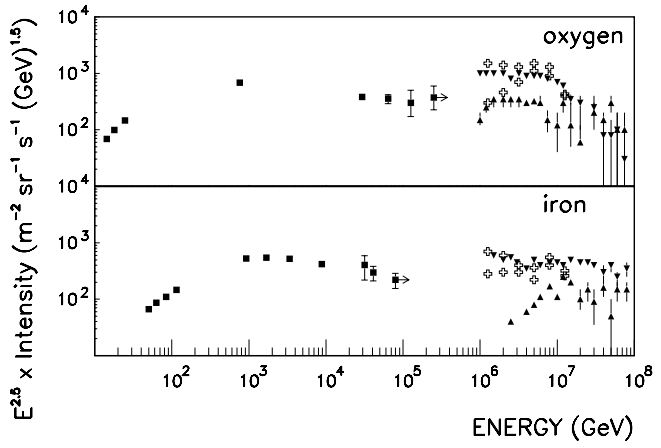

FIG. 15.—Energy spectra from TRACER (*filled squares*) compared with the interpretation of air shower data of KASCADE (*filled triangles*, for two different interaction models; Antoni et al. 2005) and of EAS-TOP (*open crosses*, two data points for each energy represent upper and lower limits; Navarra et al. 2003). The spectra are for oxygen and for iron for TRACER, but for the "CNO group" and the "Fe group" for the other observations.

fit well to an average of $\alpha = 2.65 \pm 0.05$. It must be emphasized that this result is not an artifact of the method of defining the differential intensities described in the previous sections. The similarity of the spectral shapes must indicate that acceleration and propagation mechanisms are essentially the same for all species. However, the statistical errors do not exclude the possibility of deviations from a pure power-law behavior for individual spectra.

7. COMPARISON WITH OTHER DATA

In Figure 12, the energy spectra obtained with TRACER are shown together with measurements taken in space with the HEAO-3 satellite up to ~40 GeV amu^{-1}, and with the CRN detector on the space shuttle *Challenger* up to about 1000 GeV amu^{-1}.

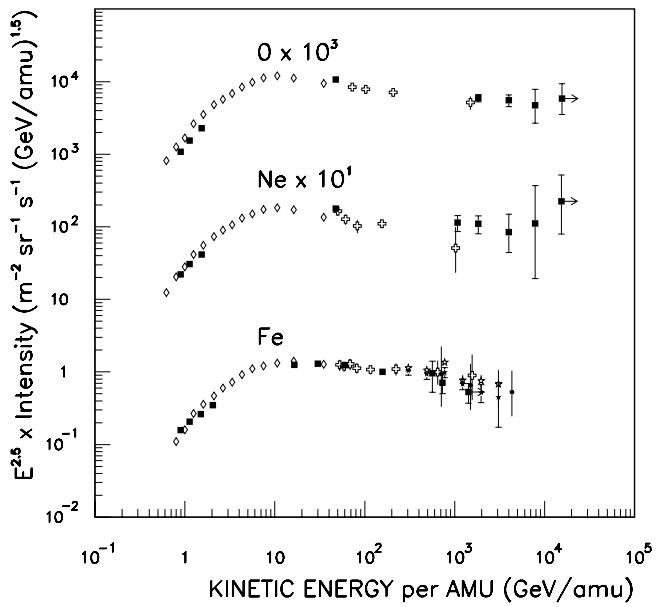

FIG. 14.—Energy spectra multiplied with $E^{2.5}$ for O, Ne, and Fe for different observations: TRACER (*filled squares*), HEAO-3 (*diamonds*; Engelmann et al. 1990), CRN (*crosses*; Müller et al. 1991), RUNJOB (*filled circles*; Derbina et al. 2005), and HESS (*open stars*: QGSJET model, and *filled stars*: SYBILL model; Aharonian et al. 2007). The error bars shown are statistical.

However, a multidecade plot such as that of Figure 12 may obscure the finer details in a steeply falling spectrum. To illustrate this, we show the energy spectra for O, Ne, and Fe in Figure 14, multiplied with $E^{2.5}$. It is apparent that the differences between individual data sets seem to be mostly statistical.

We note that Figure 14 also includes a recent determination of the high-energy iron spectrum that was performed with the HESS Imaging Air Cerenkov Telescope on the ground. Here it was possible for the first time to directly observe the Cerenkov light of iron-group nuclei in the atmosphere before they interact (Aharonian et al. 2007). Again, the agreement with the TRACER data is good, although uncertainty about the choice of a nuclear interaction model affects the interpretation of the HESS measurement.

There are also several recent or current balloon-borne detectors that are designed to obtain measurements of the high-energy cosmic-ray composition, for instance RUNJOB (Derbina et al. 2005), ATIC (Panov et al. 2006), and CREAM (Seo et al. 2008); all of these employ mostly calorimetric techniques. The RUNJOB experiment has published energy spectra mostly for groups of elements. The iron spectrum from this experiment is also included in Figure 14. Again, we see that there is good agreement with the TRACER data. Spectra for a few individual heavy elements, more limited in energy coverage and statistics than TRACER, have been reported for ATIC and CREAM at conferences (Panov et al. 2006; Ahn et al. 2007; Zei et al. 2007). These results are not included here, as they are still deemed preliminary. However, the agreement in the regions of overlap appears to be quite good.

Data for oxygen and iron from TRACER are compared in Figure 15 with spectra derived from indirect air shower observations by the EAS-TOP collaboration (Navarra et al. 2003), and by the KASCADE group for two different nucleus-nucleus interaction models (Antoni et al. 2005). These groups do not report results for individual elements: the fluxes for the "CNO group" most likely have about twice the intensity than oxygen alone, while the "iron group" is probably dominated by iron. Our results do not yet overlap with the energy region of the air shower data, but the gap is becoming smaller, in particular for oxygen. Additional measurements should indeed lead to significant constraints on the air shower interpretations.

8. CONCLUSIONS

The energy spectra of the cosmic-ray nuclei determined in this investigation extend to energies around 10^{14} eV per particle, or significantly higher for the more abundant nuclei. We believe that this data set represents the most comprehensive information about the spectra of the heavier primary nuclei currently available.

We have studied in some detail how these results provide constraints on our current understanding of the origin of Galactic cosmic rays and of models of acceleration and propagation. We realize that the upper energy limit of the measurement is still below the region of the cosmic-ray "knee," so perhaps it is not surprising that no significant changes in cosmic-ray composition are yet observed. However, the great similarity between the individual energy spectra is remarkable. The result of our studies of these features is currently being prepared for a separate publication.

It is clear that an extension of the measurements to still higher energy is desirable. The dynamic range of the TRD used here is not exhausted with the current measurement. Hence, in order to reach higher energy, the TRACER detector would either have to be increased in size, which seems impractical, as the instrument is already the largest balloon-borne cosmic-ray detector in existence, or would have to be subjected to additional long-duration balloon flights. Ideally, an instrument such as TRACER should be exposed in space for several years.

An important objective for measurements beyond the current TRACER results would be an extension of the dynamic range of the detector, such that the light secondary elements (Li, Be, B) as well as carbon and nitrogen can be covered together with the heavier nuclei. If successful to sufficiently high energies ($\sim 10^3$ GeV amu^{-1}), this measurement would lead to a determination of the L/M abundance ratio; i.e., to a determination of the propagation path length at high energy.

This would be an essential step toward a better understanding of the Galactic propagation of cosmic rays. To make this measurement possible, the electronics of TRACER have recently been completely refurbished, and another successful long-duration balloon flight was performed in 2006. The analysis of these new data is currently in progress, and results will be reported in due course.

We gratefully acknowledge the contributions of German Hermann and Scott Wakely to the design and construction of TRACER. We appreciate the services of the University of Chicago Engineering Center, especially Gary Kelderhouse, David Pernic, and Gene Drag. We thank the staff of the Columbia Scientific Balloon Facility, especially David Sullivan, and the National Science Foundation and the United States Antarctic Program for support in conducting this flight. We are indebted to Scott Cannon for his contribution in the development of the thermal protection for the instrument. This work was supported by NASA grants NAG5-5305, NN04WC08G and NNG06WC05G. M. I. acknowledges the Grant-in-Aid for Scientific Research of the Japan Society for the Promotion of Science (JSPS), No. 17540226. Numerous students have participated in the construction of the instrument under support from the Illinois Space Grant Consortium.

REFERENCES

Agostintelli, S., et al. 2003, Nucl. Instrum. Methods Phys. Res. A, 1, 250
Aharonian, F., et al. 2004, Nature, 432, 75
———. 2007, Phys. Rev. D, 75, 4
Ahn, H. S., et al. 2007, Proc. of 30th Int. Cosmic-Ray Conf. (Merida), in press
Antoni, T., et al. 2005, Astropart. Phys., 24, 1
Bell, A. R 1978, MNRAS, 182, 147
Berezhko, E. G., & Völk, H. J. 2006, A&A, 451, 981
Beuville, E., et al. 1990, Nucl. Instrum. Methods Phys. Res. A, 288, 157
Cronin, J., Gaisser, T. K., & Swordy, S. P. 1997, Sci. Am., 276, 44
Derbina, V., et al. 2005, ApJ, 628, L41
Engelmann, J., et al. 1990, A&A, 233, 96
Gahbauer, F., Hermann, G., Hörandel, J., Müller, D., & Radu, A. A. 2004, ApJ, 607, 333
Gahbauer, F., Müller, D., Hermann, G., Hörandel, J., & Radu, A. 2003, Proc. 27th Int. Cosmic-Ray Conf. (Tsukuba), 4, 2245
Garcia Muñoz, M., Mason, G. M, & Simpson, J. A 1975, ApJ, 201, L141
Heckmann, H. H., Greiner, D. E, Lindstrom, P. J., & Shwe, H. 1978, Phys. Rev. C, 17, 1735
Juliusson, E., Meyer, P., & Müller, D. 1972, Phys. Rev. Lett., 29, 445
Lagage, P. O., & Cesarsky, C. J. 1983, A&A, 125, 249
L'Heureux, J., Grunsfeld, J. M., Meyer, P., Müller, D., & Swordy, S. P. 1990, Nucl. Instrum. Methods Phys. Res. A, 295, 246
Müller, D., Swordy, S. P., Meyer, P., L'Heureux, J., & Grunsfeld, J. 1991, ApJ, 374, 356
Navarra, G., et al. 2003, Proc. 28th Int. Cosmic-Ray Conf. (Tsukuba), 1, 147
Panov, A., et al. 2006, preprint (astro-ph/0612377)
Romero-Wolf, A. 2005, M.S. thesis, Univ. Chicago
Seo, E. S., et al. 2008, Adv. Space Sci., in press
Westfall, G. D., Wilson, L. W., Lindstrom, P. J., Crawford, H. J., Greiner, D. E., & Heckman, H. H. 1979, Phys. Rev. C, 19, 1309
Wiedenbeck, M. E., et al. 1999, ApJ, 523, L61
Yanasak, N. E., et al. 2001, ApJ, 563, 768
Zei, R., et al. 2007, Proc. 30th Int. Cosmic-Ray Conf. (Merida), in press